CrossMark
click for updates

Publish Free Access

Fabrication, characterization, and optimization of a novel copper-incorporated chitosan/gelatin-based scaffold for bone tissue engineering applications

Azam Bozorgi[1], **Masoud Mozafari[1]**, **Mozafar Khazaei[2]**, **Mansooreh Soleimani[3,4]***, **Zahra Jamalpoor[5]***

[1]Department of Tissue Engineering and Regenerative Medicine, Faculty of Advanced Technologies in Medicine, Iran University of Medical Sciences, Tehran, Iran

[2]Fertility and Infertility Research Center, Health Technology Institute, Kermanshah University of Medical Sciences, Kermanshah, Iran

[3]Cellular and Molecular Research Center, Iran University of Medical Sciences, Tehran, Iran

[4]Department of Anatomy, School of Medicine, Iran University of Medical Sciences, Tehran, Iran

[5]Trauma Research Center, Aja University of Medical Sciences, Tehran, Iran

Abstract

Introduction: Fabricating composite scaffolds with improved physicochemical properties as artificial microenvironments are of great interest in bone tissue engineering. Given advantageous properties of nano-hydroxyapatite/chitosan/gelatin (nHA/Cs/Gel) scaffolds, the present study aimed to synthesize a modified nHA/Cs/Gel biomimetic scaffold with improved features.

Methods: Pure and copper (Cu)-substituted nHA was synthesized using the chemical precipitation method under controlled pH and temperature. Pure and Cu-substituted nHA/Cs/Gel scaffolds were fabricated by salt-leaching/freeze-drying method. Physicochemical characteristics of nanoparticles and scaffolds were explored using XRD, FTIR, FE-SEM/EDX, and ICP. Besides, scaffold mechanical strength, degradation, porosity, swelling, biomineralization, and cytocompatibility were assessed.

Results: Pure and Cu-substituted nHA were synthesized and characterized with appropriate Cu substitution and improved physical properties. All scaffolds were highly porous (porosity >98%) and Cu incorporation reduced porosity from 99.555 ± 0.394% to 98.69 ± 0.80% while enlarged the pore size to more than100 μm. Cu-substitution improved the scaffold mechanical strength and the best result was observed in nHA.Cu5%/Cs/Gel scaffolds by the compressive strength 88.869 ± 19.574 MPa. Furthermore, 3% and 5% Cu-substituted nHA enhanced the scaffold structural stability and supported osteoblast spread, adhesion, survival, mineralization, and proliferation. Moreover, long-term and sustainable Cu release from scaffolds was observed within 28 days.

Conclusion: Cu-substituted nHA/Cs/Gel scaffolds mimic the porous structure and mechanical strength of cancellous bone, along with prolonged degradation and Cu release, osteoblast attachment, viability, calcium deposition, and proliferation. Taken together, our results indicate the upgraded properties of nHA.Cu5%/Cs/Gel scaffolds for future applications in bone tissue engineering.
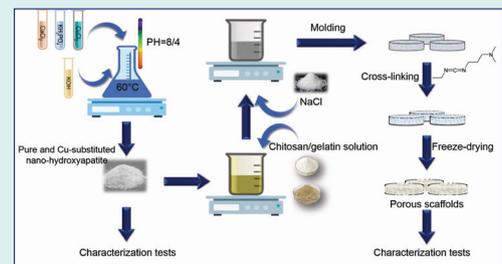
Introduction

Bone matrix is mainly composed of hydroxyapatite and type I collagen as inorganic and organic substances respectively, along with different kinds of trace elements such as iron (Fe), strontium (Sr), copper (Cu), zinc (Zn), potassium (K), and fluor (F).[1] Critical sized bone defects caused by trauma, bone tumors, and birth defects are considered as major challenges in clinics which have driven researchers to look for efficient treatments.[2] The application of autografts and allografts is the most common strategy to replace the missing bone and upgrade bone reconstruction. Autografts are known as gold standard treatments but their usage is restricted due to limited sources of bone for grafting, long periods of pain

*Corresponding authors: Mansoureh Soleimani, Email: mansourehsoleimani@gmail.com and soleimani.m@iums.ac.ir; Zahra Jamalpoor, Email: z.jamalpoor@ajaums.ac.ir and z_jamalpoor2000@yahoo.com

sufferings, and donor site complications.[3] Allografts show faster resorption,[4] increased risk of infection, and weak mechanical strength.[5] Due to these drawbacks, synthetic engineered constructs seem worthy replacements for damaged bones.

Bone tissue engineering (BTE) is a multidisciplinary field in which biomaterials, cells, and biomolecules are arranged to form three dimensional artificial microenvironments to accelerate bone regeneration. Among a variety of scaffolding biomaterials, chitosan/gelatin (Cs/Gel) based scaffolds meet desirable biomimetic hallmarks because Cs resembles the glycosaminoglycan component of bone extracellular matrix (ECM); also Gel has integrin-binding sites to facilitate cellular attachment, growth, and differentiation.[6] Cs/Gel scaffolds not only assisted with pre-osteoblast attachment, viability, and growth but also stimulated osteogenic differentiation of mesenchymal stem cells.[7] Despite advantageous biological features, a remaining challenge in the application of Cs/Gel scaffolds is their fragility and weak mechanical strength.[8]

Calcium phosphate materials are favorable additives to reinforce such polymer scaffolds among which, hydroxyapatite (HA) has gained more opportunity to develop in BTE.[9] Synthetic HA with the chemical formulation of $Ca_{10}(PO_4)_6(OH)_2$ owns physical likeness to bone HA.[10] HA nanoparticles (nHA) improve both osteogenic differentiation of pre-osteoblasts and osteoinductive properties of polymeric scaffolds.[11] A new generation of calcium phosphate materials is substituted nHA, in which trace elements such as magnesium (Mg),[13] cobalt (Co),[13] Zn,[14] Sr,[15] copper (Cu),[16] and so on are incorporated into nHA structure. Substituted nanomaterials improve physicochemical and biological properties including bioactivity, biodegradation, and positive cellular responses.[17,18] Cu-substituted calcium phosphate nanoparticles are of increasing interest because of their multifunctional features to suppress bacterial growth and ameliorate osteogenesis, biomineralization,[19] and angiogenesis.[20]

The existing studies have explored Cu incorporation into calcium phosphate scaffolds and coating[21,22] while there is limited research to look for the behavior of Cu into the highly porous structured calcium phosphate/polymer composites with prolonged ion release and appropriate biocompatibility. Besides, no previous study is available on the fabrication, characterization, and optimization of Cu-substituted nHA/Cs/Gel composite scaffolds. It is still not known whether Cu-substituted nHA has positive or negative effects on functional aspects of Cs/Gel scaffolds and how the Cu content makes a difference to the scaffold quality. Thus, the current study aimed at the synthesis and characterization of highly porous Cu-substituted nHA/Cs/Gel composite scaffolds, as well as looking over the effect of different contents of Cu substitution on physicochemical properties, Cu release behavior, and cellular responses of scaffolds.

Materials and Methods
Materials
Potassium dihydrogen phosphate (KH_2PO_4, Cat# 104873), calcium chloride anhydrous ($CaCl_2$, Cat# 102378), potassium hydroxide (KOH, Cat# 105033), Copper(II) chloride dihydrate (CuCl2, Cat# 102733), sodium chloride (NaCl, Cat# 1064060), acetic acid glacial (Cat# 101830), gelatin for microbiology (Cat# 104070), absolute ethanol (Cat# 32205), and acetone (Cat# 179124) were obtained from Merck (Merck Millipore, Darmstadt, Germany). High molecular weight chitosan (HMWC, Cat# 419419), N-(3-Dimethylaminopropyl)-N′-ethyl carbodiimide hydrochloride (EDC, Cat# E7750), phosphate-buffered saline (PBS, Cat# P4417), dimethyl sulfoxide (DMSO, Cat# D8418), glutaraldehyde 25% (Cat# G5882), ammonium hydroxide solution (NH_4OH, Cat# 221228), formaldehyde solution (36.5-38%, Cat# F8775), paraformaldehyde powder (95%, Cat# 158127), and alizarin red staining solution (40 mM, Cat# TMS-008) were purchased from Sigma (Sigma-Aldrich Chemie GmbH, Taufkirchen, Germany). Dulbecco's modified eagle medium/nutrient mixture F-12 (DMEM-F12, Cat# 10565018), fetal bovine serum (FBS, Cat# 16-000-044), penicillin-streptomycin (10,000 U/mL) (Cat# 15140122), trypsin/EDTA 0.25% (Cat# 25200056), 3-(4,5-dimethylthiazol-2-yl)-2,5-diphenyltetrazolium bromide (MTT) reagent (Cat# M6494), 4',6-diamidino-2-phenylindole (DAPI, D1306), fluorescein diacetate (FDA, Cat# F1303), and propidium iodide (PI, Cat# P3566) were acquired from Gibco (Gibco Invitrogen, Waltham, MA, USA). Osteogenic differentiation medium (Osteoplus, Cat# BI-1102) was purchased from Bioidea (Bioidea Company, Tehran, Iran). Cell culture flasks and plates were obtained from SPL (SPL Life Sciences Co., Ltd. Gyeonggi, South Korea). The human osteosarcoma cell line (Saos-2, NCBI Code: C453) was purchased from the Pasteur Institute of Iran (Tehran, Iran).

Methods
Synthesis of pure and Cu-substituted nHA
Pure nHA and a series of Cu-substituted nHA (containing Cu at 3%, 5%, and 7% of HA weight ratios) were synthesized using a chemical precipitation method described elsewhere.[23] Briefly, 0.6 M KH_2PO_4 and 1 M $CaCl_2$ were separately dissolved in deionized water and mixed while stirring at 60°C (Ca/P ratio: 1.67). In case of Cu-substituted samples, $CuCl_2$ (as Cu source) at concentrations of 2.5, 3.75, and 5 g/L was added to the stirring solution for 3%, 5%, and 7% samples respectively. The pH was adjusted at 8.4 by the dropwise addition of the 1.4 M KOH aqueous solution, meanwhile, the blend was stirred for 1 hour until precipitates were obtained. Then, the precipitates were washed with deionized water, centrifuged at 4000 rpm for 10 minutes, filtered, and dried at 60°C. Finally, nHA samples were sintered at 700°C for 1 hour in an electric furnace.

Synthesis of pure and Cu-substituted nHA/Cs/Gel scaffolds

Pure and Cu-substituted nHA/Cs/Gel scaffolds were synthesized using the salt leaching/freeze-drying technique described previously by Jamalpoor et al.[24] In a word, Cs/Gel solution was prepared by combining equal proportions (2% w/v) of HMWCs and Gel powders into the 1% (v/v) acetic acid solution in deionized water. Afterward, 1% w/v solutions of pure and Cu-substituted nHA were provided by suspending nanoparticles into the 1% (v/v) acetic acid solution, added to Cs/Gel solution and stirred for 12 hours at 40°C. Then, NaCl was added as the porogenic reagent and the blend was stirred mechanically for 72 hours. The produced paste was cast into Teflon molds and air-dried, crosslinked using the 50 mM EDC solution (48 hours), desalinated by immersing scaffolds in distilled water, and freeze-dried overnight to get final porous scaffolds for further investigations.

Characterization of nanoparticles and scaffolds

X-ray diffraction (XRD): The phase composition of nanoparticles and scaffolds was determined using Equinox 3000 X-ray diffractometer (Inel, Artenay, France), employing Cu-Kα radiation (λ=1.54187 Å) at 40 kV and 30 mA at room temperature. Data were obtained at 2ϴ ranged from 15° to 80°A with 0.03 A steps. The Rietveld refinement analyses of nanoparticles were conducted at 20°< 2ϴ <80° using Match!3 software (Crystal Impact, Bonn, Germany) to calculate a and c cell unit parameters.

Fourier transforming infrared (FTIR): The chemical structure of nanoparticles and interactions among scaffold ingredients were analyzed using the Nexus 670 ThermoNicolet Fourier transform infrared spectrometer (Thermo Electron Corporation, Gaithersburg, MD, USA). Spectrum data were collected at the range of 500 to 4000 cm^{-1} with a resolution of 0.1 cm^{-1}.

Field emission scanning electron microscopy (FE-SEM) and energy dispersive X-ray (EDX): The morphology and size of nanoparticles, and the structure and porosity of scaffolds were determined by the MIRA3TESCAN-XMU FE-SEM instrument (TESCAN ORSAY HOLDING, Brno-Kohoutovice, Czech Republic). Samples were coated with gold and analyzed at 15kV accelerating voltage. The identification of Ca, P, O, and Cu elements within samples was obtained from EDX data.

Inductively coupled plasma optical emission spectroscopy (ICP-OES): The Cu release from nanoparticles and scaffolds accomplished by immersing the same weights of samples into PBS (pH=7.4) in shaking conical tubes and incubated at 37 °C for different time points (n=3). Then, supernatants were collected, centrifuged, and Cu concentration was measured by Shimadzu ICPS S7000 (Shimadzu Corporation, Kyoto, Japan) against standard solutions of 10, 20, 50, and 100 μg/mL.

Mechanical strength: The compressive strength of scaffolds was tested by the uniaxial Instron-5566 mechanical testing machine (Instron, Norwood, MA, USA), with a 1-kN load cell. The samples were prepared with dimensions 7*14 mm, where 7 was the thickness of samples. The cross-head speed was adjusted to 1 mm/min, and the load was applied up to a 70% reduction in the initial thickness. The stress-strain curve was plotted and Young's modulus was calculated as the slope of the initial linear part of the curve (n=3).

Porosity: The porosity of scaffolds was figured using a common liquid displacement procedure by submersing scaffolds in absolute ethanol for 30 minutes followed by surface-drying and weighting (n=3). The porosity of the scaffolds was calculated using the following equation:

$$Porosity\,(\%) = \frac{W_w - W_d}{W_w - W_i}$$

Where W_d: the weight of dry samples before immersion; W_w: the weight of wet samples; W_i: the weight of submersing samples

Water uptake: The water absorption was determined by immersing scaffolds into distilled water at room temperature for different time intervals of 1, 2, 4, 6, 24, and 48 hours (n=3). The water uptake was calculated using the following equation:

$$Water\,uptake\,(\%) = \frac{W_w - W_d}{W_d} \times 100$$

Where W_d: the weight of dry scaffolds, W_w: the weight of wet scaffolds

Degradation assay: The rate of scaffold weight loss consequence to immersion into PBS at 37°C was followed-up over 4 weeks (n=4). The scaffold degradability was calculated using the following equation:

$$Degradation\,(\%) = \frac{W_0 - W_t}{W_0} \times 100$$

Where W_0: scaffold weight before immersion, W_t: scaffold weight after immersion

In vitro cellular experiments

Cell culture: Saos-2 cells were cultured in DMEM-F12 medium supplemented with 10% FBS, 100 U/mL penicillin, 100 μg/mL streptomycin, and incubated at a humidified atmosphere with 37°C temperature and 5% CO_2 pressure. The culture medium was refreshed every 3 days until cells reached 70%-80% confluency.

Cell seeding: To inspect the cell-scaffold interaction, cells were seeded on scaffolds. UV-sterilized scaffolds were transferred to 24 well cell culture plates. Saos-2 cells were detached using 0.25% trypsin/EDTA solution and resuspended at a density of 0.5×10^6 cell/mL. Then, 50 μL of cell suspension was slowly dropped on the surface of the scaffold. Thereafter, 450 μL DMEM-F12, 10% FBS medium was added to each well, and cell-seeded scaffolds were incubated at 3°C.

Cell proliferation assay: To investigate whether the materials released from the scaffold influenced the osteoblast proliferation, an indirect MTT assay was

performed by culturing Saos-2 cells in the conditioned medium (CM) from scaffolds. CM was prepared by immersing 1 mg of scaffolds into 10 mL of DMEM-F12, 10% FBS culture medium (final concentration of 100 μg/mL) followed by incubation and slow shaking at 37°C for 24 hours. Then, supernatants were collected, transferred into conical tubes, and kept at 4°C until were used. One, 3, and 7 days after that the cells were cultured in the CM, the medium was discarded and 200 μL MTT solution in PBS (0.5 mg/mL) was added to each well. The plate was incubated at 37°C for 3 hours. Then, the MTT solution was removed and 200 μL DMSO was added to dissolve formazan crystals. The absorbance of samples was measured at OD = 570 nm using an ELISA microplate reader system (Biorad, Hercules, CA, USA). Triplicates of samples were analyzed and cell proliferation was calculated according to the following equation:

$$\text{Cell proliferation (\%)} = \frac{OD_t}{OD_c} \times 100$$

Where OD_c: the OD of control cell, OD_t: the OD of cells treated with scaffold CM

Cell viability assay: Osteoblast viability was assessed qualitatively using a live-dead assay based on FDA and PI staining. For the procedure, Saos-2 cells were cultured into 48 well culture plates at a density of 1.5×10^4 cells per well and incubated in CM for 7 days. The cells cultured in DMEM-F12, 10% FBS were considered as the control group. At the end of incubation time, cells were washed with PBS, stained with FDA (5 mg/mL), and PI (2 mg/mL) dyes, and incubated for 5 minutes in the dark. After the staining solution was pulled out, cells were washed with PBS and subsequently evaluated using Optika fluorescent microscope (OPTIKA S.r.l., Ponteranica (BG), Italy).

Cell mineralization: The effect of Cu incorporation on the production of the mineralized matrix by osteoblast was assessed using the Alizarin Red S staining technique reported earlier.[25] Accordingly, 2.5×10^5 cells were seeded on scaffolds and cultured in the osteogenic differentiation medium for 7 days. Saos-2 cells cultured in polystyrene plates at the same conditions were considered as a 2D control group. After this time, culture medium was discarded, the control cells and scaffolds were washed with PBS and fixed in paraformaldehyde 4% and formalin 10% solutions in PBS respectively. Then, the fixative solutions were removed and samples were washed in distilled water and incubated in the alizarin red solution (40 mM) at room temperature for 45 minutes with gentle shaking. Afterward, the dye was excluded, specimens were washed in distilled water several times, and the dye within scaffolds was extracted by adding acetic acid 10% followed by shaking incubation at room temperature for 30 minutes. The extracted dye was collected in 1.5 mL microtubes, vortexed for 60 seconds, and heated at 85°C for 10 minutes. After being fully cooled on ice, microtubes were centrifuged at 15 000 g for 15 minutes,

the pH of dye solution was adjusted to the range of 4.1-4.5 using ammonium hydroxide 10%, and OD was measured at 405 nm in a StatFax 2100 ELISA microplate reader instrument (Awareness Technologies, Ramsey, MI, USA). Triplicates of specimens were evaluated and Alizarin red concentration was calculated against standard solutions of 250, 500, 1000, and 2000 μM.

Cell distribution: To visualize the distribution of cells within scaffolds, DAPI staining was conducted. Three days after cell seeding on scaffolds, culture media were removed, scaffolds were washed with PBS twice, 500 μL of DAPI solution in PBS (300 nM) was added to each well, and incubated for 5 minutes in the dark. Afterward, the DAPI solution was removed, scaffolds rinsed with PBS, and eventually assessed using the fluorescent microscope. Cell morphology and attachment: To observe the morphology of cells on scaffolds and cell-scaffold interaction, SEM analysis was performed. Accordingly, 3 days after cell seeding, scaffolds were washed with PBS and fixed with 2.5% glutaraldehyde for 24 hours, subsequently dehydrated using ascending grades of alcohol from 50% to 100%, and freeze-dried. Dried scaffolds were coated with gold and analyzed by TESCAN VEGA3 SEM (TESCAN ORSAY HOLDING, Brno-Kohoutovice, Czech Republic) at 30 kV accelerating voltage.

Statistical analysis
Quantitative data were gathered together in replicates mentioned previously and reported as mean ± SD. Statistical analyses were accomplished by One-way or Two-way analysis of variance (ANOVA) followed by Tukey's test in GraphPad Prism 7 software (GraphPad Software, San Diego, CA, USA) and significance levels were indicated with letters a, b, and c (a: *P* value < 0.05, b: *P* value < 0.01 and c: *P* value < 0.0001).

Results
XRD
XRD data of samples are shown in Fig. 1 (A, B). XRD patterns of nanoparticles showed a single phase of HA matching with that of JCPDS no.09-0432. Characteristic peaks of nHA and Cu-substituted samples (asterisks) were detected at 2Ɵ values: 23.1°, 26.1°, 32.2°, 33.1°, 34.4°, 40.1°, 47.1°, and 49.9°. No impurities of the CuO or CaO phase were found within nanoparticles (Fig. 1A). Evaluating lattice parameters manifested that Cu substitution imposed changes on *a* and *c* unit parameters of nHA (Table 1). *a* parameter increased in all samples while *c* parameters decreased in nHA.Cu3% and nHA.Cu5%. In addition to the presence of nHA within scaffolds (asterisks), chitosan and gelatin share the same broad peak at 2Ɵ = 20 ° (black circle), which was detected in the XRD spectrum of all scaffolds (Fig. 1B).

FTIR
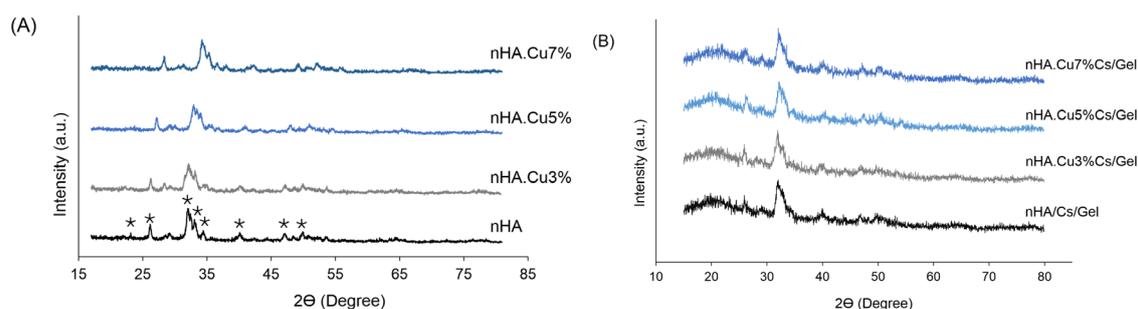FTIR patterns of nanoparticles and scaffolds are presented

Fig. 1. XRD spectra of pure and Cu-substituted nanoparticles and scaffolds. (A) the characteristic peaks of nHA were detected in all groups (asterisks) with no impurities.(B): the nHA (asterisks) and Cs/Gel (black circles) peaks were identified in scaffolds.

in Fig. 2A and 2B. Typical bonds of nHA were found within all nanoparticles with no CuO stretch (771-778 cm^{-1}) in Cu-substituted samples. Characteristic peaks included 563-565 cm^{-1}: bending of PO_4^{3-} groups, 629-633 cm^{-1}: the liberation of structural OH^- groups; 976-980 cm^{-1} and 1030-1039 cm^{-1}: PO_4^{3-} groups; 1088-1093 cm^{-1}: asymmetric stretching of PO_4^{3-} groups; 1456-1468 cm^{-1}: asymmetric stretching of CO_3^{2-} groups; 2924-2927 cm^{-1}: bending of PO_4^{3-} groups; 3400-3498 cm^{-1}: stretching vibrations of OH^- bonds belonging to adsorbed H_2O molecules; 3570-3572 cm^{-1}: stretching vibrations of OH^- groups within nHA structure (Fig. 2A). Analyzing the FTIR spectra of composite scaffolds verified the presence of bonds related to HA, Cs, Gel, and the chemical bonds between. HA peaks are around 565 cm^{-1}, 1034 cm^{-1}, and 1093 cm^{-1} noted earlier. Cs significant peaks indicated the polysaccharide content (2873 cm^{-1}: C-H asymmetric stretching and 2926 cm^{-1}: C-H symmetric stretching), N-acetyl functional groups (1345 cm^{-1}: C-N stretching of amide III, 1552 cm^{-1}: N-H deformation of amide II, and

1639-1643 cm^{-1}: C=O stretching of amide I). Moreover, a small peak of asymmetric stretching of the C-O-C group and a sharp one of N-H deformation of the primary amine group were detected. Gelatin peaks were observed at 1236 cm^{-1}: C-H stretching and N-H bending of amide III and 1448 cm^{-1}: COO groups. Moreover, additional peaks were found in association with the formation of chemical bonds between scaffold components and the cross-linking substance (EDC). Intense peaks at 1552 cm^{-1} and 1639 cm^{-1} pointed to the Cs/EDC and Gel/EDC interactions respectively. A weak peak at 1321 cm^{-1} represented the bond between COO groups of Gel with Ca ions of the nHA. There might be a weak peak of the interaction of Cu ions with chitosan and Gel at 1260 cm^{-1} overlapped with stronger peaks of Gel and nHA-Gel (Fig. 2B).

FE-SEM and EDX
The morphological assessment of nanoparticles and scaffolds is presented in Figs. 3 and 4 respectively. The appearance of the bulk mass of pure and Cu-substituted nHA particles was agglomerated and the highest agglomeration was observed in nHA.Cu7% particles. Because of dense aggregated clusters, it was difficult to evaluate the morphology of nanoparticles precisely; however, single nanoparticles detected in the view field (yellow arrows) had spherical morphologies in nanometric scales (Fig. 3A-D). FE-SEM micrographs of scaffolds (Fig. 4A-D) at the scale of 1 mm showed that a large volume of the

Table 1. Cell unit parameters of pure and Cu substituted nHA samples

Sample	nHA	nHA.Cu3%	nHA.Cu5%	nHA.Cu7%
a cell unit	9.41631	9.43948	9.43754	9.42278
c cell unit	6.8608	6.8524	6.83763	6.86401

Cell unit parameters obtained from Rietveld refinement of XRD data showed that Cu substitution increased a parameter while decreased c parameter.
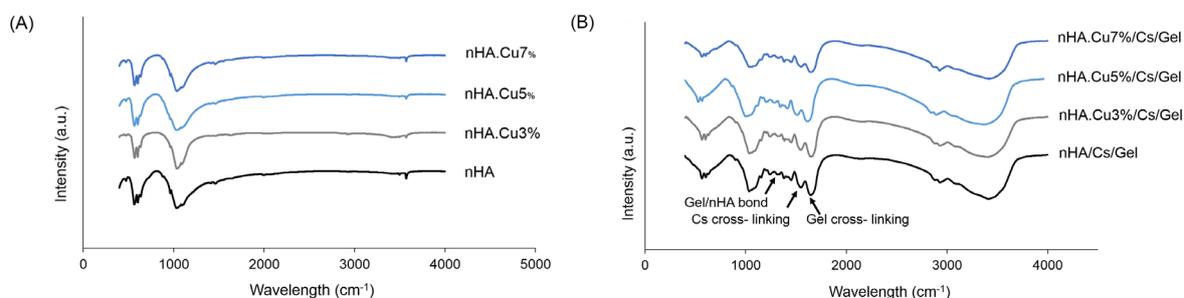

Fig. 2. FTIR spectra of pure and Cu-substituted nanoparticles and scaffolds. (A) determinant peaks of HA were detected in all nanoparticles without impure bonds. (B) the presence of nHA, Cs, and Gel were verified in the FTIR spectra of scaffolds. Moreover, chemical bonds were found between Cs/ cross-linker and Gel/ cross-linker (1552 cm^{-1} and 1639 cm^{-1} respectively) and Gel/nHA (1321 cm^{-1}).
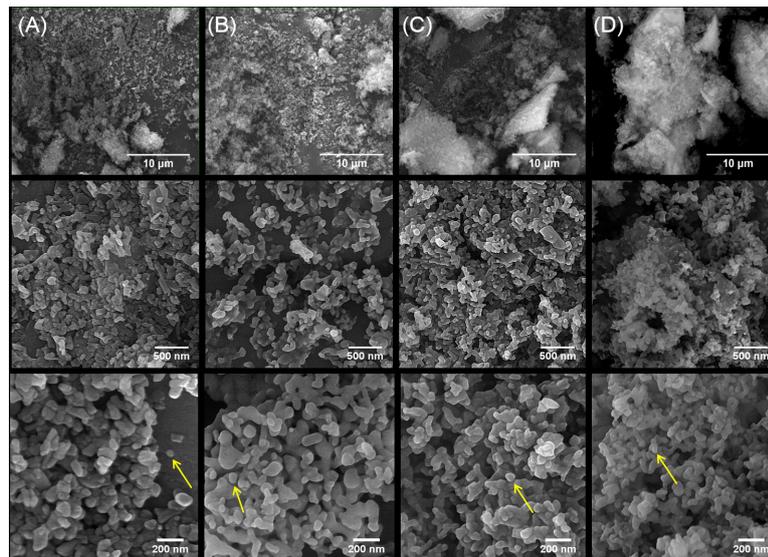
Fig. 3. FE-SEM illustrations of pure and Cu-substituted nHA. FE-SEM observations demonstrated nanoparticle agglomeration. The nanoparticles were morphologically similar to spheres; their size was distributed in a range of less than 100 nm (single nanoparticles are shown with yellow arrows).(1321 cm^{-1}).
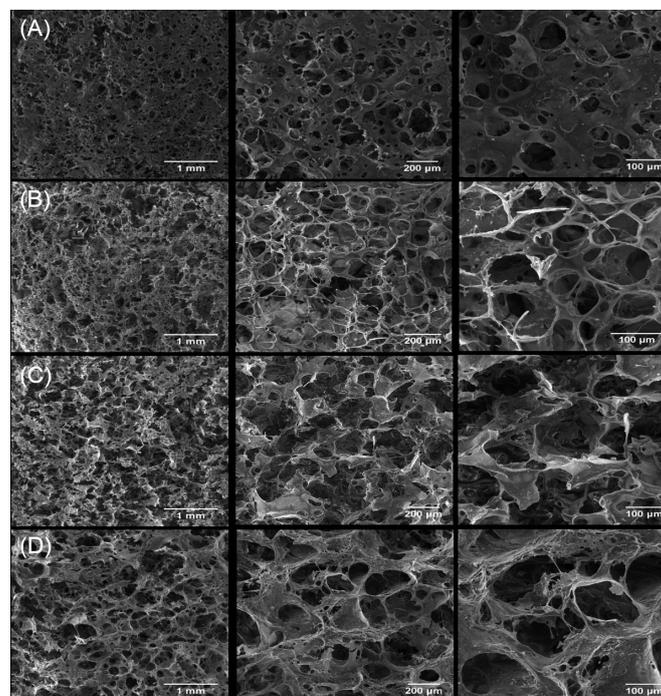

Fig. 4. FE-SEM micrographs of pure and Cu-substituted nHA/Cs/Gel scaffolds Monitoring the scaffolds by FE-SEM verified the microscopic spongy and highly porous architecture in which pores were connected to make an interconnected 3-dimensional network. The micropores were found in a variety of sizes mainly <100 μm for nHA/Cs/Gel scaffolds and >100 μm for Cu incorporated scaffolds.

scaffold was occupied by pores homogenously distributed throughout the construct. The visualization of samples at the 200 μm scale displayed the pore interconnectivity and the increment of pore size in Cu incorporated scaffolds. A more view of scaffolds at 100 μm implied that pores provide enlarged smooth walls to cellular attachment and the pore sizes of nHA/Cs/Gel scaffolds were less than 100 μm compared with Cu containing ones recognized with greater than 100 μm pores. EDX analyses expressed the existence of Ca, P, O, Cu and C, N, Ca, P, O, Cu elements

within nanoparticles and scaffolds respectively (Fig. S1A and S1B, see Supplementary file 1).

ICP

The Cu release from nanoparticles and scaffolds are presented in Fig. 5 (A, B) and Table 2. Overall, both nanoparticles and scaffolds follow a sustained release at the time points of 21 and 28 days respectively. All nanoparticles displayed a rapid release in the first week among which nHA.Cu7% release was significantly higher than others
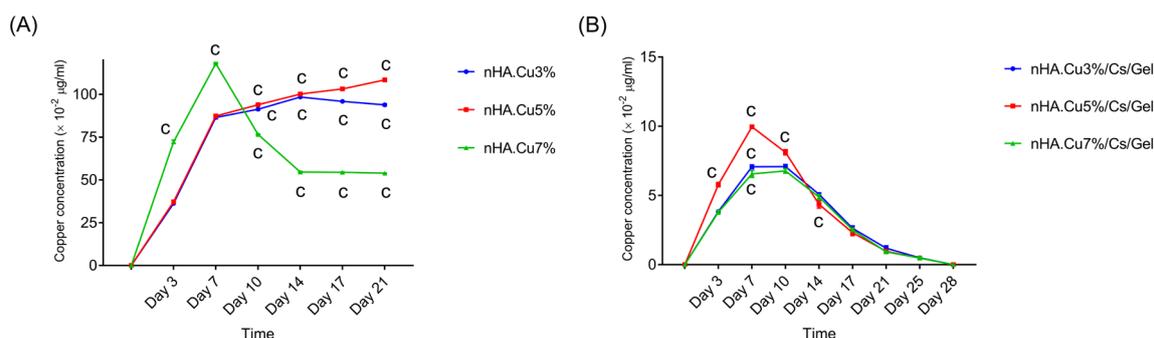
Fig. 5. The Cu release from nHA particles and nHA/Cs/Gel scaffolds. The analysis of Cu release from nanoparticles and scaffolds in different time intervals evidenced the sustained Cu release starting with the initial rapid release in the first week. (**A**) Dropping Cu release was remarked in nHA.Cu3% and nHA.Cu7% after 14 and 7 days respectively but nHA.Cu5% sample held on to slowly enhanced release. Significant levels of ion release indicated by letters were observed in nHA.Cu7% (days 3 and 7) and all groups (days 10-21) (c: *P* value < 0.001); (**B**) Scaffolds made a peak release of Cu ions from days 7 to 10 followed by gradually declined release. Significant differences were tracked in all groups (day 7) and nHA.Cu5% (days 3, 10 and 14) (c: *P* value < 0.001).

(c: *P* value<0.001). Investigating Cu release showed that each of the samples exhibited a different release pattern: nHA.Cu3% and nHA.Cu5% shared a similar behavior up to 14 days characterized by gradually increased Cu release. Since then, Cu release from nHA.Cu3% started dropping while nHA.Cu5% kept the earlier pattern until 21 days. In the case of nHA.Cu7% samples, a rapid increment in the first week, a dropped level in the second week, and a stable release in the third week were recorded. Significantly different release among all samples was reported from day 10 to the end (c: *P* value<0.001) (Fig. 5A). Despite nanoparticles, all scaffolds denoted a matching pattern of ion release depicted by increased release in the interval of 7-10 days followed by slowly declined to release up to 28 days. nHA.Cu5%/Cs/Gel scaffolds had a higher release on days 3, 10, 14, and different release was observed among all groups on day 7 (c: *P* value<0.001) (Fig. 5B).

Mechanical strength

The Young's modulus and compressive strength data of pure and Cu-substituted nHA/Cs/Gel scaffolds are attended in Fig. 6 (A, B) and Table 3. Data explained that Young's modulus and compressive strength of Cu containing scaffolds were higher than the pure scaffold.

However, significant differences were remarked among Yong's modulus of all groups (c: *P* value <0.001). nHA.Cu5%/Cs/Gel scaffolds had the greatest values of Yong's modulus and compressive strength.

Porosity

The data obtained from the liquid displacement technique in Fig. 7A confirmed that all samples were highly porous (porosity > 98%). The porosity values of pure nHA, nHA.Cu3%, nHA.Cu5%, and nHA.Cu7% incorporated scaffolds are 99.555 ± 0.394%, 99.182 ± 0.185%, 99.245 ± 0.23%, and 98.69 ± 0.80% respectively. Cu incorporation caused the decreased porosity associating with the amount of Cu incorporated into nHA (no significant difference).

Water uptake

Evaluating the swelling potential of scaffolds showed that all groups had a strong potential to absorb water over 48 hours of assessment (Fig. 7B). Significant differences in water uptake were registered among all groups at all times (c: *P* value<0.001) except nHA.Cu3% and nHA.Cu5% containing scaffolds at 6 hours. Data inferred that water uptake was significantly reduced following Cu incorporation. The most water absorption for pure

Table 2. Cu concentration of nanoparticles and scaffolds over 21 and 28 days of assessment

Time	Cu concentration (× 10⁻² μg.mL) (mean ± SD)					
	Nanoparticles			**Scaffolds**		
	nHA.Cu3%	**nHA.Cu5%**	**nHA.Cu7%**	**nHA.Cu3%.Cs.Gel**	**nHA.Cu5%.Cs.Gel**	**nHA.Cu7%.Cs.Gel**
Day 3	36.26 ± 0.176	37.23 ± 0.306	72.31 ± 097	3.84 ± 0.07	5.78 ± 0.148	3.79 ± 0.125
Day 7	86.48 ±0.701	87.3 ± 0.200	118.02 ± 0.475	7.07 ± 0.131	9.955 ± 0.09	6.56 ± 0.245
Day 10	91.31 ± 0.412	93.956 ± 0.649	76.56 ± 0.3	7.08 ± 0.151	8.12 ± 0.181	6.77 ± 0.161
Day 14	98.45 ±0.180	100.163 ± 0.207	54.6 ± 0.297	5.08 ± 0.104	4.35 ± 0.264	4.88 ± 0.177
Day 17	95.91 ± 0.177	103.186 ± 0.260	54.51 ± 0.151	2.62 ± 0.172	2.306 ± 0.211	2.516 ± 0.121
Day 21	93.9 ± 0.608	108.486 ± 0.727	53.96 ± 0.091	1.2 ± 0.16	0.96 ± 0.121	0.925 ± 0.009
Day 25	-	-	-	0.49 ± 0.062	0.47 ± 0.032	0.476 ± 0.091
Day 28	-	-	-	0	0	0

Table 3. Young's modulus and compressive strength values of pure and Cu- substituted nHA/Cs/Gel scaffolds

Sample	nHA/Cs/Gel	nHA.Cu3%/Cs/Gel	nHA.Cu5%/Cs/Gel	nHA.Cu7%/Cs/Gel
Young's modulus (MPa)	1.009 ± 0.0026	1.282 ± 0.0107	1.325 ± 0.0121	1.033 ± 0.022
Compressive strength (MPa)	78.155 ± 11.99	84.923 ± 15.173	88.869 ± 19.574	77.577 ± 5.253

nHA, nHA.Cu5% and nHA.Cu7% containing scaffolds was recorded following 24 hours whereas that of nHA. Cu3% containing samples was one hour. nHA.Cu5%/Cs/Gel scaffolds hold a better water uptake potency in comparison to nHA.Cu3% and nHA.Cu7% ones.

Degradation

The weight loss ratio of scaffolds following the immersion into PBS solution is depicted in Fig. 8A, data revealed that all groups exhibited proper degradation by 38.94 ± 4.54% for nHA/Cs/Gel, 21.44 ± 4.23% for nHA.Cu3%/Cs/Gel, 32.7 ± 3.8% for nHA.Cu35%/Cs/Gel, and 40 ± 1.95% for nHA.Cu7%/Cs/Gel scaffolds over 28 days. The degradation of Cu3% and Cu5%-substituted nHA incorporated scaffolds was lower than pure nHA samples at all periods. A significantly diminished degradation rate was observed in nHA.Cu3%/Cs/Gel scaffolds on day 28 (day 28, c: P value <0.001). However, nHA.Cu7%/Cs/Gel scaffolds appeared the reverse event by significantly increased degradation rate on all periods (c: P value <0.001, a: P value < 0.05, n: non-significant).

Cell mineralization

The qualitative and quantitative data of the Alizarin Red S staining method in Fig. 8 (B, C) demonstrated that both pure and Cu-substituted nHA/Cs/Gel scaffolds remarkably enhanced the mineralization of Saos-2 cells cultured in osteogenic differentiation medium within 7 days compared to those cultured in 2D culture plates. Cu-substituted nHA incorporated scaffolds displayed more calcium deposition than pure ones among which, nHA.Cu5%/Cs/Gel samples were notably different (c: P value <0.001). The descending order of mineralization was as follows: nHA.Cu5%/Cs/Gel (1216.75 ± 78.5 μM)
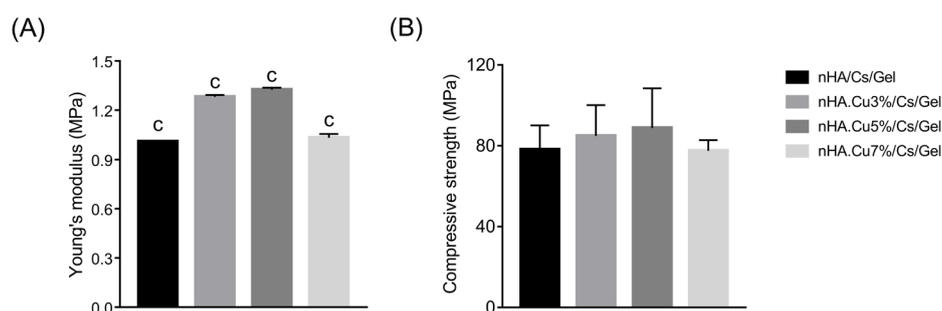

Fig. 6. Young's modulus and compressive strength of pure and Cu-substituted nHA/Cs/Gel scaffolds. (A) Young's moduli of Cu containing scaffolds were significantly higher than nHA/Cs/Gel scaffold (c: P value<0.001). There were significant differences among all groups (c: P value<0.001) and nHA.Cu5%/Cs/Gel scaffold owned the highest Young's modulus. (B) the compressive strength values of Cu incorporated scaffolds were greater than nHA/Cs/Gel samples among which, nHA.Cu5%/Cs/Gel scaffold possessed the greatest one (no significant difference).
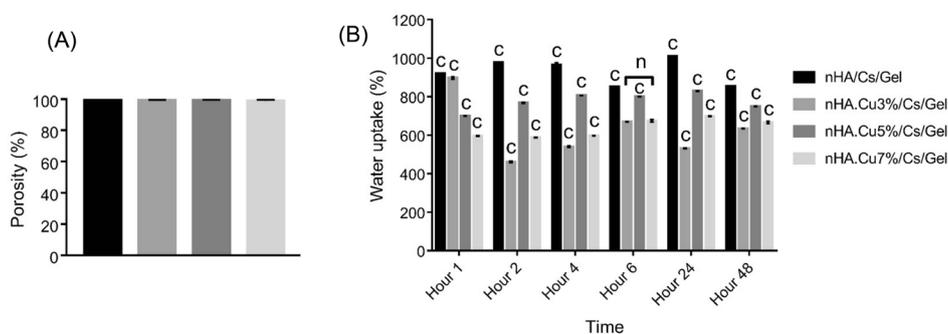

Fig. 7. The porosity and water uptake of pure and Cu- substituted nHA/Cs/Gel scaffolds. (A) the porosity assessment denoted that all groups were highly porous (> 98%). The porosity of Cu incorporated scaffolds was lower vs nHA/Cs/Gel ones (no significant difference). (B) water uptake data referred to the intense capacity of scaffolds to uptake water and swell. Cu incorporated scaffolds showed a considerably decreased water uptake in contrast to Cu-free scaffolds at all times (c: P value<0.001). There was no significant difference in the water uptake potential of nHA.Cu3%/Cs/Gel and nHA.Cu7%/Cs/Gel groups at 6 hours (n: non-significant).
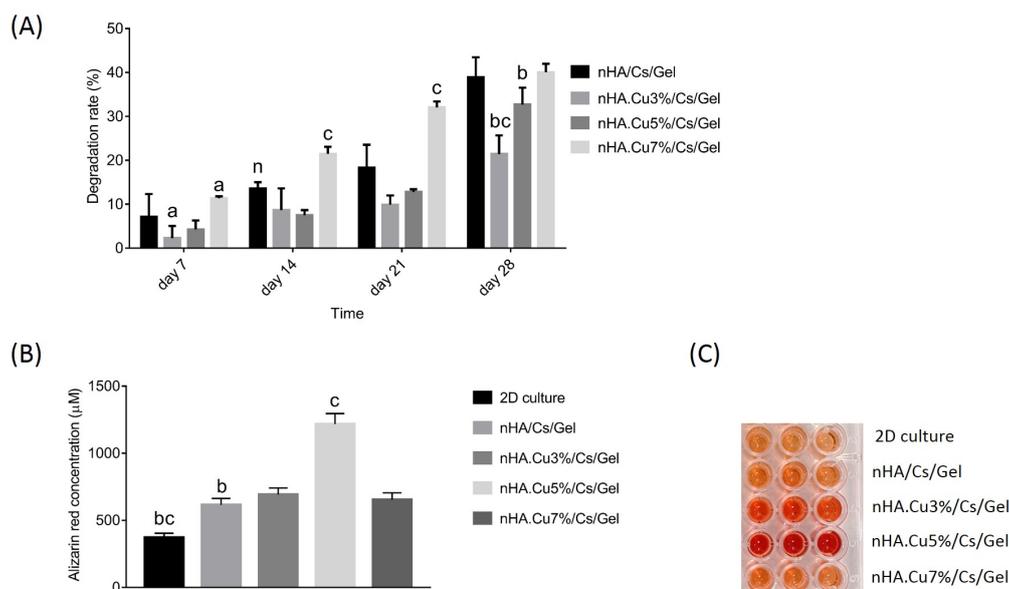
Fig. 8. The degradability and osteoblast mineralization of pure and Cu- substituted nHA/Cs/Gel scaffolds. **(A)** the degradation rate of scaffolds was assessed in 28 days by immersing scaffolds into PBS solution (pH = 7.4, 37°C). Data revealed that scaffolds containing nHA.Cu3% and nHA.Cu5% concerned lower degradation rates in comparison to nHA/Cs/Gel scaffolds while nHA.Cu7% had a higher degradability (c: Pvalue<0.001, b: P value<0.01, a: Pvalue<0.05, n: non-significant). **(B)** and **(C)** the quantitative analysis of alizarin red staining following the culture of osteoblasts on scaffolds over 7 days showed that both pure and Cu-substituted nHA/Cs/Gel scaffolds increased the osteoblast mineralization compared to those cultured on polystyrene plates (c: Pvalue<0.001, b: Pvalue<0.01). Cu incorporated scaffolds displayed higher mineralization in comparison with pure nHA/Cs/Gel scaffolds. The most increased osteoblast mineralization was observed in Cu5% containing scaffolds and there were significant differences between all groups but nHA/Cs/Gel with nHA.Cu3% /Cs/Gel and nHA.Cu7% /Cs/Gel groups.

> nHA.Cu3%/Cs/Gel (692.23 ± 49.12 μM) > nHA.Cu7%/Cs/Gel (653.63 ± 51.13 μM) > pure nHA/Cs/Gel (615.03 ± 47.8 μM) > 2D culture (369.8 ± 34.3 μM). There were no significant differences among pure, Cu3%, and Cu7% -substituted nHA/Cs/Gel experimental groups (c: P value <0.001, b: P value <0.01).

Cell proliferation

Fig. 9A represents the effect of scaffold CM on Saos-2 osteoblast proliferation measured by MTT assay. The data showed that CM from nHA.Cu3% and nHA.Cu5% scaffolds positively influenced cell proliferation by 114.54 ± 12.15% and 117.28 ± 16% on day 1 while pure and nHA. Cu7% samples declined it by 93.72 ± 9.66% and 8.47 ± 10.2% respectively (b: P value <0.01, a: P value <0.05). On day 3, the cell proliferation of experimental groups was enhanced (129.8 ± 8.1% for nHA/Cs/Gel, 116.55 ± 13.5% for nHA.Cu3%/Cs/Gel, 116 ± 13% for nHA.Cu5%/Cs/Gel, 112.4 ± 2/6% for nHA.Cu7%/Gel) but the significant increase was only observed in nHA/Cs/Gel CM (a: P value <0.05). On day 7, CM from nHA/Cs/Gel, Cu3%/Cs/Gel, and nHA.Cu5%/Cs/Gel scaffolds notably promoted osteoblast proliferation in the order already mentioned by 159.3 ± 16%, 134.6 ± 4.2%, and 127.4 ± 12.94% (c: P value <0.001, b: P value <0.01) whereas that of nHA.Cu7%/Cs/Gel scaffolds remarkably reduced to 68.32 ± 5.65% (c: P value <0.001).

Cell viability

The live dead staining data are shown in Fig. 9B. FDA/PI live-dead assay was utilized to explore the cytotoxic effect of Cu content on Saos-2 cell viability. Living cells uptake non-fluorescent FDA dye and convert it into fluorescent green fluorescein. Instead, the nuclei of dead cells are stained with PI in red color. Illustrations announced that large proportions of cells were alive and high concentrations (100 μg/mL) of pure and Cu-substituted nHA/Cs/Gel scaffolds CM did not induce toxic effects on Saos-2 osteoblasts and supported cell survival over 7 days of culture.

Cell distribution

The images from DAPI staining in Fig. 10A displayed that cells successfully attached to the scaffolds, penetrated, and distributed into the scaffolds within 3 days after being seeded on the surface of scaffolds. It is noteworthy that DAPI-stained cells look sharper attached to the superficial surfaces while others did to the deeper parts. In some regions, scaffold was stained with DAPI appearing as blue stains in the image background (yellow arrow).

Cell morphology

SEM micrographs 3 days after osteoblasts were cultured on scaffolds in Fig. 10B showed that scaffolds had appropriate structural stability in the biological fluid, cells successfully attached to the pore wall and expanded their cytoplasmic projections known as filopodia (yellow arrows) indicating approving scaffold cytocompatibility. Fig. 10C showed the morphological appearance of FDI/PI stained Saos-2 cells
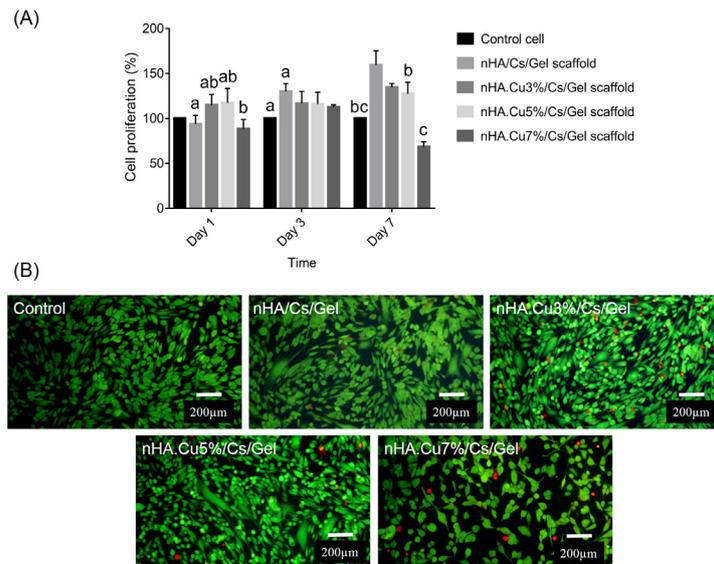
(A)

(B)

Fig. 9. The effect of pure and Cu- substituted nHA/Cs/Gel scaffold conditioned media (CM) on Saos-2 osteoblast proliferation and viability. **(A)** MTT results illustrated that CM from nHA.Cu3%/Cs/Gel and nHA.Cu5%/Cs/Gel scaffolds significantly affected osteoblast proliferation on days 1 (b P value <0.01, a: P value < 0.05), and 3 (for nHA.Cu3%/Cs/Gel scaffold, a: P value < 0.05). A positive correlation was found between osteoblast growth and scaffolds but nHA. Cu7%/Cs/Gel scaffolds (c: P value < 0.001, b P value <0.01, a: P value < 0.05). **(B)** the live dead staining on day 7 exhibited a high number of live cells (green) vs dead ones (red) indicating desirable osteoblast viability exposed to scaffold CM.
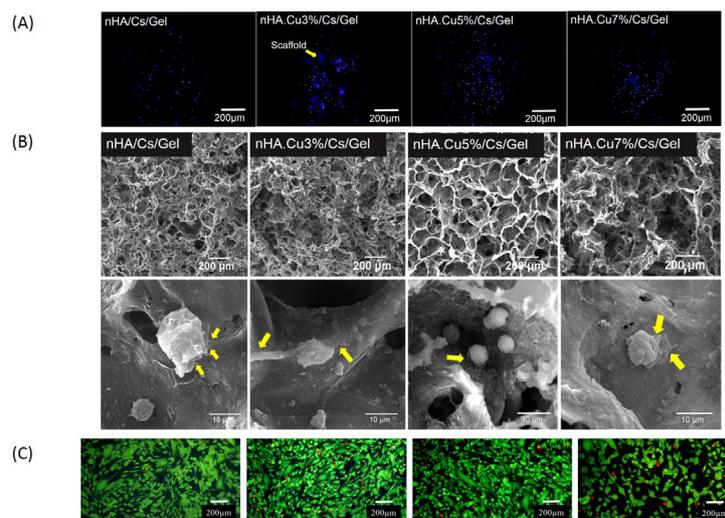
(A)

(B)

(C)

Fig. 10. The distribution and morphology of Saos-2 osteoblasts within pure and Cu- substituted nHA/Cs/Gel scaffolds. **(A)** DAPI staining images presented the spread of osteoblasts within scaffolds. Cells that reside in regions near the surface of the scaffold seemed sharper while those distributed into deeper parts were blurred. The stained scaffolds were observable in the background (yellow arrow). **(B)** SEM images of cells seeded on scaffolds after 3 days showed that cells were able to attach to the scaffold pore walls, extend filopodia (yellow arrows) reflecting scaffold cytocompatibility.

cultured on polystyrene plates treated with scaffold CM for 7 days (data are the same described in Fig. 9B).

Discussion

Recently, developing a new generation of porous chitosan-based composite scaffolds with the potency of sustained ion release and ameliorated physicochemical properties have attracted more attention.[26] Copper, an essential trace element of bone matrix, improves the angiogenic and osteogenic properties of BTE scaffolds. However, the fabrication of scaffolds with optimized content of Cu

considers demanding issues to discuss.[27] We previously reported the synthesis of the nHA/Cs/Gel composite scaffold with optimized Cs/Gel ratios.[28] In the present study, we first focused on the Cu substitution into HA nanoparticles at different weight ratios, and in the next step, we compared the effect of Cu incorporation on the physico/chemical characteristics of HA/Cs/Gel composite scaffolds and the corresponding biological responses of osteoblasts.

Structural analyses of pure and Cu- substituted HA nanoparticles by XRD were in agreement with JCPDS

no.09-0432 indicating a single phase of hydroxyapatite with lattice parameters close to previous reports (Table 1).[29] Cu incorporation was found to expand a, and decline c parameters. The decreased a parameter could be referred to as Cu substitution for Ca ions; the lower ionic radius of Cu ions (0.73 Å versus 0.99 Å of calcium ions) leads a parameter to reduce.[30,31] Increased cell unit parameters are justifiable in consideration of enhanced content of lattice H_2O confirmed with FTIR peaks at 3570-3572 cm^{-1}.[32] At a higher level of Cu incorporation (7% wt), dehydroxylation of materials might lead to a small decrease in a parameter expansion.[33] XRD spectra demonstrated the existence of nHA, Cs, and Gel components within scaffolds. Little amounts of CO_3 found in FTIR patterns of nanoparticles (1456-1468 cm^{-1}) form due to the interaction of CO_2 molecules in the air with Ca and Cu ions located on the surface of apatite crystals.[30] FTIR peaks at 1552 cm^{-1} and 1639 cm^{-1} definite that new bonds were formed following the interaction of Cs and Gel with the cross-linking reagent (EDC).[34] EDC molecules activate the carboxylic acid functional groups of Gel structure to subsequently interact with amine groups of Cs.[35] A peak at 1321 cm^{-1} reflects the chemical bond between carboxylic groups of gelatin with Ca ions of nHA, rising the mechanical strength of the scaffold.[36]

It can be seen from FE-SEM images that nanoparticles are agglomerated at the dry state and the degree of agglomeration increases with Cu incorporation. Although it is difficult to measure nanoparticles size and shape by FE-SEM because of high agglomeration, it is suggested that the increased nanoparticle aggregation could be due to the decreased size of nanoparticles as a function of Cu substitution.[16] It is interpreted from observations that there are no notable differences in the shape of nanoparticles in various groups. Single nanoparticles appear in spherical shapes with sizes less than 100 nm. Nanospheres and nanorods are less cytotoxic compared to other forms of nHA[37] and ameliorate the MC3T3-E1 osteoblast growth.[38] The observational assessments reveal that scaffolds are highly porous involving an interconnected network of micropores in which pores are found in a range of micrometer scales. Cu-substituted nHA incorporated scaffolds have greater pores compared to pure nHA incorporated ones mainly more than 100 μm in size. Copper ions have smaller ionic radii and consequently larger charge density than calcium ions leading to the formation of stronger ionic interactions between copper ions and carboxyl groups of other scaffold components. These interactions are impressive in giving rise to larger pore sizes.[39] The scaffold porosity is a determining factor in cell migration, proliferation, and vascularization and the pore size of 100-200 μm provides appropriate space for bone ingrowth.[40]

EDX data showed the elemental composition of samples and confirmed the presence of Ca, P, and Cu ions (Fig. 6). The Ca/P atomic ratio of nHA was close to the theoretical values of stoichiometric nHA (1.67) and natural bone (1.75) reflecting the biomimetic nature of synthesized nanoparticles.[41] Furthermore, incorporating Cu into nHA gives rise to the decreased ratio of Ca/P, which could be attributed to calcium deficiency and substitution of Cu ions for Ca ions.[42] ICP data approve the moderate release of Cu ions from nanoparticles and scaffolds for 21 and 28 days respectively. Long term Cu release may favor the improvement of osteogenesis and angiogenesis.[43] Our findings infer that the more Cu concentration in the curation solution, the more initial Cu release from substituted nanoparticles is observed. Those groups containing lower amounts of Cu (3% and 5% Cu) follow a more stable release within 21 days. In contrast, The Cu release from scaffolds takes place independently from the initial Cu concentration. For example, as described in Table 2, the highest Cu release from nHA.Cu3%/Cs/Gel and nHA.Cu5%/Cs/Gel scaffolds were 7/08 ± 0.151 × 10^{-2} μg/mL (day 10) and 9/955 ± 0.09 × 10^{-2} μg/mL (day 7) respectively while that of nHA.Cu7%/Cs/Gel scaffolds was 6/77 ± 0.161 × 10^{-2} μg/mL on day 10. The contradicted data of nanoparticles and scaffolds could rely on the availability of Cu ions in nanoparticles that easily exchange with PBS while those of scaffolds are trapped within the scaffold by interactions with other components.[44] Mechanical strength is a crucial aspect of BTE scaffolds and constructs with suitable compressive strength endow osteoconductive and osteoinductive features mediated by osteoblast mechanotransduction.[45] Mechanical test data point to the enhanced mechanical strength of Cu-substituted nHA/Cs/Gel scaffolds. Cu incorporation approaches the mechanical strength of scaffolds to that of trabecular bone (100-150 MPa).[46] The highest mechanical strength was observed in the Cu5% group but the Cu7% group had a reduced compressive strength. This data was in agreement with that reported by Ai et al. reasoned that higher Cu contents prevent the nHA crystallization and crystal growth, thereby diminishing the scaffold compressive strength.[47]

The diminished degradability is expected as reported earlier[48] and is in agreement with mechanical test results in which the weight loss of Cu3% and Cu5% containing scaffolds are lower than pure and Cu7% incorporated specimens. From the obtained results, it is inferred that there is a reverse correlation between scaffold structural stability and degradation. Cu incorporation is supposed to stabilize the nHA chemical bond with Gel at 3% and 5% contents characterized by FTIR. In the case of nHA.Cu7%/Cs/Gel scaffolds, it seems that large pore size creates a large surface area[49] that in conjugation with lower mechanical strength accelerates the degradation rate. The porosity of Cu containing scaffolds is lower than that of pure samples followed by the decreased water uptake. Although the water uptake potential of scaffolds decreased with Cu incorporation, all experimental groups showed excellent water uptake more than 200% appropriate to

bone regeneration.[50] nHA.Cu5%/Cs/Gel scaffolds show a better swelling ratio due to the higher porosity and strong interactions of Cu ions with hydrophilic functional groups of scaffold components. Radwan-Pragłowska et al implied that the interaction of water molecules with hydrophilic free functional groups causes scaffold pores to reduce.[51] We hypothesized that the greater pore size, as well as the more compact structure of Cu incorporated scaffolds due to stronger interactions of nHA and Gel, are decisive to reduced porosity and water uptake respectively.

As well, we investigated the osteoblast response to materials released from scaffolds into the culture medium. To coordinate the Cu release data with those of the MTT assay, we used the same amounts of scaffolds that were assessed for Cu release. Therefore, we conclude that the conditioned medium of 100 µg/mL of HA and the Cu3% and Cu5%- substituted samples strongly upgrade the proliferation of Saos-2 cells on days 3 and 7 in comparison with the control group, a result by a study showing the stimulatory effect of brushite, a precursor of HA on MG63 cells activity and proliferation.[52] The suggested mechanism by which Cu ions trigger cell proliferation is related to the activation of Atox1.[53] Furthermore, we negotiate that scaffolds bearing Cu ions harm osteoblast growth compared to pure nHA/Cs/Gel scaffolds. Previous studies intimate that Cu ions have both proliferative and anti-proliferative effects in a time and dose-dependent manner[54] and our finding was along with that reported by Yang et al, evidenced the lower Cu release the more reduced pre-osteoblast proliferation is observed.[55] We compared the cell proliferation data with Cu ion release from scaffolds and found that osteoblast growth is directly dependent on the Cu ion concentration. Though the antiproliferative mechanism of Cu ions at low concentrations has not been well discussed, dropping levels of Cu ions might induce oxidative stress and reduced superoxide dismutase activity.[56] To expand our knowledge of the challenging information on the toxic effect of Cu ions,[54, 57] we performed live-dead staining to detect whether Cu ions induce cytotoxicity. FDA/PI staining images show higher numbers of both viable and dead cells compared to the control group in scaffold groups, reflecting the negligible toxic nature of scaffolds. Our results confirmed the higher levels of mineral deposition in 3D scaffolds when compared with osteoblasts cultured in 2D polystyrene plates. nHA was previously found to enhance the calcium and protein adsorption potential of Cs/Gel composite networks.[58] Moreover, nHA refines the production of osteocalcin by osteoblasts coupled with enhanced mineralized matrix secretion.[59] Cu incorporated scaffolds showed higher calcium deposition of osteoblasts than Cu-free samples, data were in coordination with previous reports.[54, 60] We perceived that osteoblast mineralization was directly correlated to the released Cu ions, not the initial amount of Cu incorporated into scaffolds. The Cu release from nHA.Cu5%/Cs/Gel

Research Highlights

What is the current knowledge?
√ nHA/Cs/Gel scaffolds are considered as a widely used composite scaffold for BTE applications.
√ Low concentrations of Cu upgrade the structural pore size, mechanical strength, osteoblast viability, proliferation, and mineralization of nHA/Cs/Gel scaffolds.

What is new here?
√ Cu-substituted nHA incorporated Cs/Gel composite scaffolds provide highly porous 3D constructs with promising physicochemical properties, mechanical strength, sustained Cu release, and osteoblast attachment, proliferation, and mineralization. However, higher concentrations of Cu ions imped scaffold physicochemical properties and cellular response.

scaffold was strongly higher than that in other groups $(9/955 \pm 0.09 \times 10^{-2}\text{µg/mL})$. Cu ions drive osteoblasts to produce the mineralized matrix as a result of collagen synthesis.[61] The highly porous scaffolding architecture and appropriate pore size mimic the microstructure of spongy bone that permits the uniform distribution of cells within the scaffold,[62] the attachment of cells to the pore walls, followed by expansion and proliferation.

Conclusion

In the current study, we designed a two-step experiment for synthesis and qualification of highly porous pure and Cu-substituted nHA/Cs/Gel scaffolds using a simple salt leaching/ freeze-drying method. Further investigation demonstrated that different components of scaffolds interact with each other to make a three-dimensional network of interconnected micropores. Cu- incorporated scaffolds have the potential to release Cu ions over a long term period along with improved mechanical strength, microstructure, pore size, and degradation behavior *in vitro*. Moreover, they provide an appropriate environment to support osteoblast homogenous spread, survival, attachment, proliferation, and mineralized matrix production. However, the Cu content is an impressive parameter to determine the physico/chemical and biological aspects of scaffolds. In summary, we assume that nHA.Cu5%/Cs/Gel scaffolds possess optimized properties comparable to other groups and could be proper candidates for BTE applications but more experiments seem necessary to uncover the osteogenic and angiogenic potential of Cu incorporated scaffolds.

Ethical statement

None to be declared.

Competing interests

The authors declare that there is no conflict of interests with the present manuscript.

Authors' contribution

AB: Investigation, data curation, writing original draft. MM: Conceptualization, methodology, validation. MK: Data analysis, writing - review and editing. MS: Supervision, project administration, funding acquisition, provision of study materials and equipment. ZJ: Supervision, project administration, experiments design, writing - review and editing.

Supplementary Materials

Supplementary file 1 contains Figure S1.

References

1. Eliaz N, Metoki N. Calcium phosphate bioceramics: a review of their history, structure, properties, coating technologies and biomedical applications. *Materials* **2017**; 10: 334.

2. Pierrie SN, Hsu JR. Shortening and Angulation Strategies to Address Composite Bone and Soft Tissue Defects. *J Orthop Trauma* **2017**; 31 Suppl 5: S32-s5. https://doi.org/10.1097/bot.0000000000000976

3. Sheikh Z, Najeeb S, Khurshid Z, Verma V, Rashid H, Glogauer M. Biodegradable Materials for Bone Repair and Tissue Engineering Applications. *Materials (Basel)* **2015**; 8: 5744-94. https://doi.org/10.3390/ma8095273

4. Galindo-Moreno P, de Buitrago JG, Padial-Molina M, Fernandez-Barbero JE, Ata-Ali J, F OV. Histopathological comparison of healing after maxillary sinus augmentation using xenograft mixed with autogenous bone versus allograft mixed with autogenous bone. *Clin Oral Implants Res* **2018**; 29: 192-201. https://doi.org/10.1111/clr.13098

5. Sohn HS, Oh JK. Review of bone graft and bone substitutes with an emphasis on fracture surgeries. *Biomater Res* **2019**; 23: 9. https://doi.org/10.1186/s40824-019-0157-y

6. Olad A, Hagh HBK. Graphene oxide and amin-modified graphene oxide incorporated chitosan-gelatin scaffolds as promising materials for tissue engineering. *Composites Part B: Engineering* **2019**; 162: 692-702.

7. Georgopoulou A, Papadogiannis F, Batsali A, Marakis J, Alpantaki K, Eliopoulos AG, *et al.* Chitosan/gelatin scaffolds support bone regeneration. *J Mater Sci Mater Med* **2018**; 29: 59. https://doi.org/10.1007/s10856-018-6064-2

8. Vlasceanu GM, Crica LE, Pandele AM, Ionita M. Graphene oxide reinforcing genipin crosslinked chitosan-gelatin blend films. *Coatings* **2020**; 10: 189.

9. Shakir M, Zia I, Rehman A, Ullah R. Fabrication and characterization of nanoengineered biocompatible n-HA/chitosan-tamarind seed polysaccharide: Bio-inspired nanocomposites for bone tissue engineering. *Int J Biol Macromol* **2018**; 111: 903-16. https://doi.org/10.1016/j.ijbiomac.2018.01.035

10. Posner AS. Crystal chemistry of bone mineral. *Physiol Rev* **1969**; 49: 760-92. https://doi.org/10.1152/physrev.1969.49.4.760

11. Lei X, Gao J, Xing F, Zhang Y, Ma Y, Zhang G. Comparative evaluation of the physicochemical properties of nano-hydroxyapatite/collagen and natural bone ceramic/collagen scaffolds and their osteogenesis-promoting effect on MC3T3-E1 cells. *Regen Biomater* **2019**; 6: 361-71. https://doi.org/10.1093/rb/rbz026

12. Stipniece L, Stepanova V, Narkevica I, Salma-Ancane K, Boyd AR. Comparative study of surface properties of Mg-substituted hydroxyapatite bioceramic microspheres. *Journal of the European Ceramic Society* **2018**; 38: 761-8.

13. Birgani ZT, Gharraee N, Malhotra A, van Blitterswijk CA, Habibovic P. Combinatorial incorporation of fluoride and cobalt ions into calcium phosphates to stimulate osteogenesis and angiogenesis. *Biomed Mater* **2016**; 11: 015020. https://doi.org/10.1088/1748-6041/11/1/015020

14. Shepherd D, Best SM. Production of zinc substituted hydroxyapatite using various precipitation routes. *Biomed Mater* **2013**; 8: 025003. https://doi.org/10.1088/1748-6041/8/2/025003

15. Frasnelli M, Cristofaro F, Sglavo VM, Dirè S, Callone E, Ceccato R, *et al.* Synthesis and characterization of strontium-substituted hydroxyapatite nanoparticles for bone regeneration. *Materials Science and Engineering: C* **2017**; 71: 653-62.

16. Othmani M, Bachoua H, Ghandour Y, Aissa A, Debbabi M. Synthesis, characterization and catalytic properties of copper-substituted hydroxyapatite nanocrystals. *Materials Research Bulletin* **2018**; 97: 560-6.

17. Ahmed M, Mansour S, Mostafa MS, Darwesh R, El-dek S. Structural, mechanical and thermal features of Bi and Sr co-substituted hydroxyapatite. *J Mater Sci* **2019**; 54: 1977-91.

18. Gomes S, Vichery C, Descamps S, Martinez H, Kaur A, Jacobs A, *et al.* Cu-doping of calcium phosphate bioceramics: From mechanism to the control of cytotoxicity. *Acta Biomater* **2018**; 65: 462-74. https://doi.org/10.1016/j.actbio.2017.10.028

19. Lu Y, Li L, Zhu Y, Wang X, Li M, Lin Z, *et al.* Multifunctional Copper-Containing Carboxymethyl Chitosan/Alginate Scaffolds for Eradicating Clinical Bacterial Infection and Promoting Bone Formation. *ACS Appl Mater Interfaces* **2018**; 10: 127-38. https://doi.org/10.1021/acsami.7b13750

20. Bejarano J, Detsch R, Boccaccini AR, Palza H. PDLLA scaffolds with Cu- and Zn-doped bioactive glasses having multifunctional properties for bone regeneration. *J Biomed Mater Res A* **2017**; 105: 746-56. https://doi.org/10.1002/jbm.a.35952

21. Wang C, Jin K, He J, Wang J, Yang X, Yao C, *et al.* Synergistic Effect of Copper-Containing Mesoporous Bioactive Glass Coating on Stimulating Vascularization of Porous Hydroxyapatite Orbital Implants in Rabbits. *J Biomed Nanotechnol* **2018**; 14: 688-97. https://doi.org/10.1166/jbn.2018.2513

22. Erol MM, Mouriňo V, Newby P, Chatzistavrou X, Roether JA, Hupa L, *et al.* Copper-releasing, boron-containing bioactive glass-based scaffolds coated with alginate for bone tissue engineering. *Acta Biomater* **2012**; 8: 792-801. https://doi.org/10.1016/j.actbio.2011.10.013

23. Shanmugam S, Gopal B. Copper substituted hydroxyapatite and fluorapatite: synthesis, characterization and antimicrobial properties. *Ceramics International* **2014**; 40: 15655-62.

24. Jamalpoor Z, Mirzadeh H, Joghataei MT, Zeini D, Bagheri-Khoulenjani S, Nourani MR. Fabrication of cancellous biomimetic chitosan-based nanocomposite scaffolds applying a combinational method for bone tissue engineering. *J Biomed Mater Res A* **2015**; 103: 1882-92. https://doi.org/10.1002/jbm.a.35320

25. Brennan M, Renaud A, Gamblin AL, D'Arros C, Nedellec S, Trichet V, *et al.* 3D cell culture and osteogenic differentiation of human bone marrow stromal cells plated onto jet-sprayed or electrospun micro-fiber scaffolds. *Biomed Mater* **2015**; 10: 045019. https://doi.org/10.1088/1748-6041/10/4/045019

26. Gritsch L, Maqbool M, Mouriño V, Ciraldo FE, Cresswell M, Jackson PR, *et al.* Chitosan/hydroxyapatite composite bone tissue engineering scaffolds with dual and decoupled therapeutic ion delivery: copper and strontium. *J Mater Chem B* **2019**; 7: 6109-24. https://doi.org/10.1039/c9tb00897g

27. Liu C, Fu X, Pan H, Wan P, Wang L, Tan L, *et al.* Biodegradable Mg-Cu alloys with enhanced osteogenesis, angiogenesis, and long-lasting antibacterial effects. *Sci Rep* **2016**; 6: 27374. https://doi.org/10.1038/srep27374

28. Jamalpoor Z, Mirzadeh H, Joghataei MT, Zeini D, Bagheri-Khoulenjani S, Nourani MR. Fabrication of cancellous biomimetic chitosan-based nanocomposite scaffolds applying a combinational method for bone tissue engineering. *J Biomed Mater Res A* **2015**; 103: 1882-92. https://doi.org/10.1002/jbm.a.35320

29. Gibson IR, Bonfield W. Novel synthesis and characterization of an AB-type carbonate-substituted hydroxyapatite. *J Biomed Mater Res* **2002**; 59: 697-708. https://doi.org/10.1002/jbm.10044

30. Stanić V, Dimitrijević S, Antić-Stanković J, Mitrić M, Jokić B,

Plećaš IB, *et al.* Synthesis, characterization and antimicrobial activity of copper and zinc-doped hydroxyapatite nanopowders. *Applied Surface Science* **2010**; 256: 6083-9.

31. Sumathi S, Gopal B. Copper substituted hydroxyapatite and fluorapatite: Synthesis, characterization and antimicrobial properties. *Ceramics International* **2014**; 40: 15655-62. https://doi.org/10.1016/j.ceramint.2014.07.086

32. Zhang H, Zhao C, Wen J, Li X, Fu L. Synthesis and structural characteristics of magnesium and zinc doped hydroxyapatite whiskers. *Ceram Silik* **2017**; 61: 244-9.

33. Ehret C, Aid-Launais R, Sagardoy T, Siadous R, Bareille R, Rey S, *et al.* Strontium-doped hydroxyapatite polysaccharide materials effect on ectopic bone formation. *PLoS One* **2017**; 12: e0184663. https://doi.org/10.1371/journal.pone.0184663

34. Ji Yin Y, Zhao F, Feng Song X, De Yao K, Lu WW, Chiyan Leong J. Preparation and characterization of hydroxyapatite/chitosan–gelatin network composite. *Journal of Applied Polymer Science* **2000**; 77: 2929-38. https://doi.org/10.1002/1097-4628(20000923)77:13<2929::aid-app16>3.0.co;2-q

35. Bagheri-Khoulenjani S, Mirzadeh H, Etrati-Khosroshahi M, Shokrgozar MA. Development of a method for measuring and modeling the NH2 content and crosslinking density of chitosan/gelatin/nanohydroxyapatite based microspheres. *Polymer Testing* **2016**; 51: 20-8. https://doi.org/10.1016/j.polymertesting.2016.01.019

36. Maji K, Dasgupta S, Pramanik K, Bissoyi A. Preparation and Evaluation of Gelatin-Chitosan-Nanobioglass 3D Porous Scaffold for Bone Tissue Engineering. *International Journal of Biomaterials* **2016**; 2016: 9825659. https://doi.org/10.1155/2016/9825659

37. Zhao Y, Zhang Y, Ning F, Guo D, Xu Z. Synthesis and cellular biocompatibility of two kinds of HAP with different nanocrystal morphology. *J Biomed Mater Res B Appl Biomater* **2007**; 83: 121-6. https://doi.org/10.1002/jbm.b.30774

38. Zhang H, Qing F, Zhao H, Fan H, Liu M, Zhang X. Cellular internalization of rod-like nano hydroxyapatite particles and their size and dose-dependent effects on pre-osteoblasts. *J Mater Chem B* **2017**; 5: 1205-17. https://doi.org/10.1039/c6tb01401a

39. Lu Y, Li L, Zhu Y, Wang X, Li M, Lin Z, *et al.* Multifunctional Copper-Containing Carboxymethyl Chitosan/Alginate Scaffolds for Eradicating Clinical Bacterial Infection and Promoting Bone Formation. *ACS Appl Mater Interfaces* **2018**; 10: 127-38. https://doi.org/10.1021/acsami.7b13750

40. Karageorgiou V, Kaplan D. Porosity of 3D biomaterial scaffolds and osteogenesis. *Biomaterials* **2005**; 26: 5474-91. https://doi.org/10.1016/j.biomaterials.2005.02.002

41. Geçer A, Yıldız N, Erol M, Çalımlı A. Synthesis of chitin calcium phosphate composite in different growth media. *Polymer Composites* **2008**; 29: 84-91. https://doi.org/10.1002/pc.20385

42. Ofudje EA, Adeogun AI, Idowu MA, Kareem SO. Synthesis and characterization of Zn-Doped hydroxyapatite: scaffold application, antibacterial and bioactivity studies. *Heliyon* **2019**; 5: e01716.

43. Mou P, Peng H, Zhou L, Li L, Li H, Huang Q. A novel composite scaffold of Cu-doped nano calcium-deficient hydroxyapatite/multi-(amino acid) copolymer for bone tissue regeneration. *Int J Nanomedicine* **2019**; 14: 3331-43. https://doi.org/10.2147/ijn.s195316

44. Bari A, Bloise N, Fiorilli S, Novajra G, Vallet-Regí M, Bruni G, *et al.* Copper-containing mesoporous bioactive glass nanoparticles as multifunctional agent for bone regeneration. *Acta Biomaterialia* **2017**; 55: 493-504. https://doi.org/10.1016/j.actbio.2017.04.012

45. Prasadh S, Wong RCW. Unraveling the mechanical strength of biomaterials used as a bone scaffold in oral and maxillofacial defects. *Oral Science International* **2018**; 15: 48-55. https://doi.org/10.1016/S1348-8643(18)30005-3

46. Roohani-Esfahani S-I, Newman P, Zreiqat H. Design and Fabrication of 3D printed Scaffolds with a Mechanical Strength Comparable to Cortical Bone to Repair Large Bone Defects. *Sci Rep* **2016**; 6: 19468. https://doi.org/10.1038/srep19468

47. Ai F, Chen L, Yan J, Yang K, Li S, Duan H, *et al.* Hydroxyapatite scaffolds containing copper for bone tissue engineering. *Journal of Sol-Gel Science and Technology* **2020**; 95: 168-79. https://doi.org/10.1007/s10971-020-05285-0

48. Kumari S, Singh BN, Srivastava P. Effect of copper nanoparticles on physico-chemical properties of chitosan and gelatin-based scaffold developed for skin tissue engineering application. *3 Biotech* **2019**; 9: 102. https://doi.org/10.1007/s13205-019-1624-9

49. Wu L, Ding J. Effects of porosity and pore size on in vitro degradation of three-dimensional porous poly (D, L-lactide-co-glycolide) scaffolds for tissue engineering. *J Biomed Mater Res A* **2005**; 75: 767-77.

50. Qu H, Fu H, Han Z, Sun Y. Biomaterials for bone tissue engineering scaffolds: a review. *RSC Advances* **2019**; 9: 26252-62. https://doi.org/10.1039/C9RA05214C

51. Radwan-Pragłowska J, Janus Ł, Piątkowski M, Bogdał D, Matysek D. 3D Hierarchical, Nanostructured Chitosan/PLA/HA Scaffolds Doped with TiO(2)/Au/Pt NPs with Tunable Properties for Guided Bone Tissue Engineering. *Polymers (Basel)* **2020**; 12. https://doi.org/10.3390/polym12040792

52. Ewald A, Käppel C, Vorndran E, Moseke C, Gelinsky M, Gbureck U. The effect of Cu(II)-loaded brushite scaffolds on growth and activity of osteoblastic cells. *J Biomed Mater Res A* **2012**; 100: 2392-400. https://doi.org/10.1002/jbm.a.34184

53. Itoh S, Kim HW, Nakagawa O, Ozumi K, Lessner SM, Aoki H, *et al.* Novel role of antioxidant-1 (Atox1) as a copper-dependent transcription factor involved in cell proliferation. *J Biol Chem* **2008**; 283: 9157-67.

54. Zhang X, Li J, Wang X, Wang Y, Hang R, Huang X, *et al.* Effects of copper nanoparticles in porous TiO2 coatings on bacterial resistance and cytocompatibility of osteoblasts and endothelial cells. *Mater Sci Eng C Mater Biol Appl* **2018**; 82: 110-20. https://doi.org/10.1016/j.msec.2017.08.061

55. Yang L, Perez-Amodio S, Barrère-de Groot FYF, Everts V, van Blitterswijk CA, Habibovic P. The effects of inorganic additives to calcium phosphate on in vitro behavior of osteoblasts and osteoclasts. *Biomaterials* **2010**; 31: 2976-89. https://doi.org/10.1016/j.biomaterials.2010.01.002

56. Kardos J, Héja L, Simon Á, Jablonkai I, Kovács R, Jemnitz K. Copper signalling: causes and consequences. *Cell Communication and Signaling* **2018**; 16: 71. https://doi.org/10.1186/s12964-018-0277-3

57. Li Y, Ho J, Ooi CP. Antibacterial efficacy and cytotoxicity studies of copper (II) and titanium (IV) substituted hydroxyapatite nanoparticles. *Mater Sci Eng C* **2010**; 30: 1137-44. https://doi.org/10.1016/j.msec.2010.06.011

58. Zhao F, Grayson WL, Ma T, Bunnell B, Lu WW. Effects of hydroxyapatite in 3-D chitosan–gelatin polymer network on human mesenchymal stem cell construct development. *Biomaterials* **2006**; 27: 1859-67. https://doi.org/10.1016/j.biomaterials.2005.09.031

59. Deschaseaux F, Sensébé L, Heymann D. Mechanisms of bone repair and regeneration. *Trends Mol Med* **2009**; 15: 417-29.

60. Ryan EJ, Ryan AJ, González-Vázquez A, Philippart A, Ciraldo FE, Hobbs C, *et al.* Collagen scaffolds functionalised with copper-eluting bioactive glass reduce infection and enhance osteogenesis and angiogenesis both in vitro and in vivo. *Biomaterials* **2019**; 197: 405-16. https://doi.org/10.1016/j.biomaterials.2019.01.031

61. Weng L, Boda SK, Teusink MJ, Shuler FD, Li X, Xie J. Binary Doping of Strontium and Copper Enhancing Osteogenesis and Angiogenesis of Bioactive Glass Nanofibers while Suppressing Osteoclast Activity. *ACS Appl Mater Interfaces* **2017**; 9: 24484-96. https://doi.org/10.1021/acsami.7b06521

62. Zhang K, Fan Y, Dunne N, Li X. Effect of microporosity on scaffolds for bone tissue engineering. *Regen Biomater* **2018**; 5: 115-24. https://doi.org/10.1093/rb/rby001